



# Static and dynamic contact angles of evaporating liquids on heated surfaces

Vladimir S. Ajaev<sup>a,\*</sup>, Tatiana Gambaryan-Roisman<sup>b,c</sup>, Peter Stephan<sup>b,c</sup>

<sup>a</sup> Department of Mathematics, Southern Methodist University, Dallas, TX 75275, United States

<sup>b</sup> Chair of Technical Thermodynamics, Technische Universität Darmstadt, Petersenstr. 30, 64287 Darmstadt, Germany

<sup>c</sup> Center for Smart Interfaces, Technische Universität Darmstadt, Petersenstr. 32, 64287 Darmstadt, Germany

## ARTICLE INFO

### Article history:

Received 16 June 2009

Accepted 17 October 2009

Available online 1 November 2009

### Keywords:

Viscous flows

Evaporation

Contact lines

Disjoining pressure

Thermocapillary flow

## ABSTRACT

We studied both static and dynamic values of the apparent contact angle for gravity-driven flow of a volatile liquid down a heated inclined plane. The apparent contact line is modeled as the transition region between the macroscopic film and ultra-thin adsorbed film dominated by disjoining pressure effects. Four commonly used disjoining pressure models are investigated. The static contact angle is shown to increase with heater temperature, in qualitative agreement with experimental observations. The angle is less sensitive to the details of the disjoining pressure curves than in the isothermal regime. A generalization of the classical Frumkin–Derjaguin theory is proposed to explain this observation. The dynamic contact angle follows the Tanner's law remarkably well over a range of evaporation conditions. However, deviations from the predictions based on the Tanner's law are found when interface shape changes rapidly in response to rapid changes of the heater temperature. The Marangoni stresses are shown to result in increase of the values of apparent contact angles.

© 2009 Elsevier Inc. All rights reserved.

## 1. Introduction

It is well known from the studies of adsorption that a very thin film, referred to as an adsorbed film, can form on a solid surface in contact with vapor phase [1,2]. Thus, a liquid–vapor interface which appears to be in contact with a solid surface can in fact be in contact with this adsorbed film so that there is no true three-phase contact line. Models of contact lines on heated surfaces based on this assumption were developed in the pioneering works of Potash and Wayner [3] and Moosman and Homsy [4]. These authors consider a steady meniscus on a uniformly heated surface. The adsorbed film does not evaporate despite the fact that the substrate is above the saturation temperature due to the effects of the so-called disjoining pressure [2]. This contribution to the stresses in ultra-thin films effectively shifts the conditions of thermodynamic equilibrium at the liquid–vapor interface. As a result, the evaporation from the adsorbed film is suppressed. The models of Potash and Wayner [3] and Moosman and Homsy [4] describe the profile of the vapor–liquid interface in the vicinity of the apparent contact line. Macroscopic shape of the vapor–liquid interface has to match the adsorbed-film solution asymptotically. The contact line is then described as the region of rapid change of interfacial curvature where such matching takes place. The approach has been used successfully for finding local steady-state solutions near contact lines on heated surfaces [5,6]. A similar approach has been

used by Lyushnin et al. [7] in their studies of dewetting in thin films of polar liquids.

The effects of heat conduction in the solid have been included in the description of steady menisci by Stephan and Busse [8]. The authors have developed a two-dimensional model describing the heat transfer in a grooved heat pipe evaporator. This model combines the solution of heat conduction problem in the groove wall with the computation of the profile of the ultra-thin liquid film in the vicinity of the apparent contact line. It has been shown that the evaporation rate in the vicinity of the apparent contact line contributes to up to 50% of the total evaporation rate from the groove.

The mathematical models of evaporation near contact lines developed by Potash and Wayner [3] and Stephan and Busse [8] were motivated mostly by experimental work on heat pipes. However, similar approaches can be applied to a range of other experimental configurations, such as thin-film flow under the action of gravity, which is the focus of the present work. This basic configuration has been subject of several recent experimental studies motivated by applications in cooling of electronic devices [9–11]. It also provides useful insights into dynamics of other flows driven by body forces, most notably in spin coating process developed for manufacture of integrated circuits and more recently used for fabrication of compact disks and DVDs. Finally, the present study is relevant for understanding the dynamics of contact lines during droplet evaporation [12], an important process for spray cooling and biological applications, as well as the dynamics of menisci and vapor bubbles in microchannels [13,14].

\* Corresponding author. Fax: +1 214 768 2355.

E-mail address: ajaev@mail.smu.edu (V.S. Ajaev).

The governing equations for fluid flow and heat transfer are well understood so the main challenges for mathematical modeling have to do with imposing proper boundary conditions for these equations. Numerical simulations of moving liquid–vapor interfaces often rely on fixed contact angle condition at the apparent contact line [14]. However, experimental observations [3,12] indicate that the apparent contact angle can deviate significantly from the equilibrium static value due to evaporation and contact line motion. A clear understanding of how the contact angle depends on local temperature and contact line speed is essential for formulating an effective-contact-angle condition for numerical simulations of two-phase flows with evaporation. Such condition would lead to better agreement between numerical and experimental results for a range of applications without the need to resolve the details of small-scale phenomena taking place near the apparent contact line. This motivated us to focus our investigation on the values of the apparent contact angle and their dependence on surface properties and temperature of the solid wall and contact line velocity.

It is known that in the absence of evaporation the apparent contact angle depends on the spreading velocity of the contact line. Voinov [15] and Tanner [16] have used hydrodynamic theory to show that for perfectly wetting liquid/solid systems the dynamic contact angle  $\Phi_D$  is related to the contact line velocity  $V$  by a power law:  $\Phi_D^3 \sim \mu V / \sigma$ , where  $\mu$  is the dynamic viscosity of the liquid and  $\sigma$  is the surface tension. This relation has been validated by comparison with the experiments of Hoffman [17] on displacement of air by silicon oils in glass capillaries. The above relation between the apparent dynamic contact angle and the contact line velocity, following the suggestion of Hoffman [17], has been extended to the cases of partial wetting. It can be represented in the form of the Hoffman–Voinov–Tanner law (often referred to as Tanner's law) [18]:

$$\Phi_D^3 = \Phi^3 + c_T \frac{\mu V}{\sigma}, \quad (1)$$

where  $\Phi$  denotes the equilibrium contact angle. The empirical constant  $c_T$  is close to 72 [17]. The validity of this formula in the presence of evaporation has not been addressed in the literature.

The effect of evaporation on moving contact lines has been studied by Ajaev et al. [19,20] in the context of oscillating bubbles and coating flows. In the latter work a gravity-driven coating flow of a volatile liquid down a heated inclined plane was considered. It was shown that the apparent contact angle increased with increasing the contact line speed and with increasing of the evaporation rate.

All evaporation models described above (except [7]) are based on an assumption that the disjoining pressure results from the repulsive van der Waals forces and therefore has the form  $\Pi \sim 1/h^3$ , where  $h$  is the dimensional film thickness. This form of the disjoining pressure corresponds to liquids which are perfectly wetting on the given surface under isothermal conditions (although evaporation may result in a measurable apparent contact angle). However, there are many practical applications and experimental studies in which the contact angle, even though small, is not zero. In particular, water, which is of interest for many heat transfer applications, is partially wetting on many surfaces. Thus, one cannot in general expect the van der Waals type models of disjoining pressure to be in quantitative agreement with experiments for partially wetting evaporating liquids. This was recently demonstrated in experiments of Soddke et al. [12] which clearly showed that the one-component model of disjoining pressure systematically underpredicts the values of the apparent contact angle. This study pointed to an important gap in modeling literature: the lack of understanding of the effect of two-component disjoining pressure on contact lines in the presence of evaporation. The goal

of the present paper is to fill this gap by generalizing the approaches of Moosman and Homsy [4] and Ajaev et al. [19,20] to the case of partial wetting. The results are illustrated using the example of volatile liquid sliding along a heated inclined solid plane, which has been previously studied by Ajaev [20] for the case of a perfectly wetting liquid. The results will be used for establishing a correlation between the apparent contact angle, the contact line velocity and the parameters related to evaporation.

When the contact angle is nonzero, there is more than one component of disjoining pressure determining its value and the common van der Waals based law of  $1/h^3$  is no longer applicable. Experimentally, disjoining pressure curves look similar to the one sketched in Fig. 1. We consider a situation when adsorbed film is present, but the apparent contact angle is not zero. Several different models have been used to describe such behavior. They fall into three major categories: (a) a combination of two different inverse power laws [21–23], (b) the standard van der Waals terms with an additional exponential contribution [24] and (c) an approximate formula used by Wong et al. [25]. Several models take into account the dependence of the disjoining pressure not only on film thickness, but also on the slope and the curvature of the interface [26–29].

The equilibrium contact angle  $\Phi$  can be calculated from the known disjoining pressure using the Frumkin–Derjaguin theory [30]. They have used energy balance to obtain the following relation:

$$\cos \Phi = 1 + \frac{1}{\sigma} \int_{h_0}^{\infty} \Pi(h) dh, \quad (2)$$

where  $h_0$  is the thin wetting layer thickness, which can be determined from the equation  $\Pi(h_0) = 0$ . Eq. (2) is valid for drops and menisci of a large curvature radius.

We use a lubrication-type approach which relies on the assumption of liquid film thickness being small compared to all other macroscopic length scales in the problem. This approach has been used for a variety of gravity-driven flows over solid surfaces [31,32]; its validity has been discussed by Goodwin and Homsy [33] and Mazouchi et al. [34].

We introduce a model of moving contact lines in the presence of phase change based on the ideas from earlier work on steady menisci in contact with heated surfaces by Potash and Wayner [3] and Moosman and Homsy [4]. We incorporate different models of disjoining pressure which enable the description of the finite contact angle in stationary isothermal meniscus [21,23,25]. We simulate numerically the evolution of the shape of the liquid–vapor interface in a gravity-driven coating flow of an evaporating liquid. The results of these simulations are used for determination of profiles of the evaporating liquid film in the vicinity of the moving contact

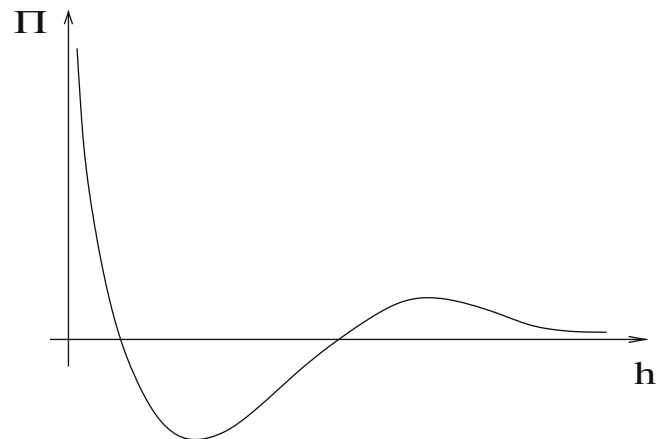


Fig. 1. Sketch of a typical disjoining pressure curve.

line for different forms of the disjoining pressure and for quantification of the relationship between the contact angle, contact line velocity and the evaporation rate.

## 2. Mathematical model

### 2.1. Formulation

We consider flow of a volatile viscous liquid of density  $\rho$  and viscosity  $\mu$  on a heated solid surface, as shown in Fig. 2a. The solid surface is at an angle  $\alpha$  to the horizontal direction. The nondimensional temperature profile along the surface, shown in Fig. 2b, simulates a finite-size heater; temperature is scaled by the equilibrium saturation temperature,  $T_s^*$ . The main physical effects of heating on the gravity-driven flow are the mass loss at the vapor–liquid interface due to evaporation and the thermocapillary stress. The latter is acting along the interface which can no longer be considered isothermal in the presence of heating.

The solution far away from the leading edge of the advancing vapor–liquid interface is assumed to be a parallel viscous flow in a film of uniform thickness  $b$ , which is used as the scale for all length variables in this section. The governing equations for nondimensional liquid velocity  $\mathbf{v}$ , pressure  $p$ , and temperature  $T$  are written in the form

$$-\frac{1}{C}\nabla p + \nabla^2 \mathbf{v} + \mathbf{e}_g = 0, \quad (3)$$

$$\nabla \cdot \mathbf{v} = 0, \quad (4)$$

$$\nabla^2 T = 0. \quad (5)$$

Here  $\mathbf{e}_g$  is the unit vector in the direction of gravity. We use the capillary scale,  $\sigma_0/b$ , for the pressure, where  $\sigma_0$  is the surface tension at the temperature  $T_s^*$ . The velocity scale  $U$  is the characteristic velocity of the parallel gravity-driven flow away from the contact line [34],

$$U = \frac{\rho g b^2}{\mu}, \quad (6)$$

where  $g$  is the acceleration of gravity; time is scaled with  $b/U$ . We introduce the capillary number according to

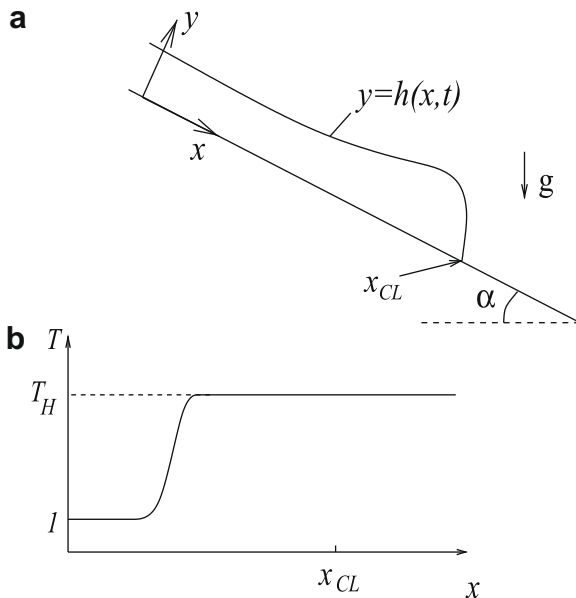


Fig. 2. Sketch of gravity driven viscous flow of a volatile liquid on an inclined heated surface (a) and the scaled temperature profile along the solid substrate (b).

$$C = \frac{\mu U}{\sigma_0}.$$

Both inertia effects and convective heat transfer are assumed negligible. The fluid flow in the vapor phase directly above the liquid is in general coupled to the flow in the liquid. However, in this study we use the one-sided model of evaporation [35]. It implies that the density, dynamic viscosity, and thermal conductivity of the vapor phase are very small compared to those of the liquid. Therefore, we take the limit when the corresponding nondimensional ratios approach zero. However, the vapor density is retained in the boundary conditions where it multiplies the vapor velocity, which can be large.

Let us define the evaporation number according to

$$E = \frac{kT_s^*}{\rho U \mathcal{L} b},$$

where  $k$  is the thermal conductivity of the liquid,  $\mathcal{L}$  is the latent heat of vaporization; the characteristic velocity  $U$  is defined by Eq. (6) above. The evaporation number is the ratio of the timescale of the downward gravity driven motion of the liquid to the evaporative timescale. We note that the definition of the evaporation number in the present work is similar to that used in [20] and different from that in Burelbach et al. [35] where a viscous velocity scale,  $\mu/\rho b$ , is used instead of Eq. (6).

The nondimensional conditions of conservation of mass and energy at the liquid–vapor interface are

$$Ej = (\mathbf{v} - \mathbf{v}^l) \cdot \mathbf{n}, \quad (7)$$

$$J = -\mathbf{n} \cdot \nabla T - \beta(T - 1). \quad (8)$$

Here  $\mathbf{n}$  is the unit normal vector to the interface pointing into the vapor,  $\mathbf{v}^l$  is the velocity of the interface, and the scaled mass flux at the liquid–vapor interface is defined as

$$J = J^* \mathcal{L} b / kT_s^*,$$

where  $J^*$  is the dimensional mass flux.  $\beta$  denotes the Biot number, which characterizes the heat loss to the vapor.

The normal and shear stress balances at the interface are written in the form

$$\mathbf{n} \cdot \mathbf{T} \cdot \mathbf{n} = \nabla \cdot \mathbf{n} + \Pi_0 - p_v, \quad (9)$$

$$\mathbf{t} \cdot \mathbf{T} \cdot \mathbf{n} = -Mt \cdot \nabla T. \quad (10)$$

Here  $p_v$  is the scaled vapor pressure, and the condition (10) is satisfied for any tangent vector  $\mathbf{t}$ . The nondimensional stress tensor,  $\mathbf{T}$ , and disjoining pressure,  $\Pi_0$ , are the ratios of corresponding dimensional quantities to the capillary pressure scale,  $\sigma_0/b$ . We also assume that the surface tension is a linear function of temperature,

$$\sigma = \sigma_0 - \gamma(T^* - T_s^*),$$

and introduce the modified Marangoni number  $M = \gamma T_s^* / \sigma_0$ . The interfacial temperature  $T^i$  is related to the local mass flux and pressure jump at the interface through the non-equilibrium condition [36] written in the form:

$$Kj = \delta(p - p_v) + T^i - 1, \quad (11)$$

where

$$K = \frac{kT_s^*}{2\rho_v \mathcal{L}^2 b} \sqrt{2\pi \bar{R} T_s^*}, \quad \delta = \frac{\sigma_0}{\mathcal{L} \rho b}.$$

Here  $\bar{R}$  is the gas constant per unit mass,  $\rho_v$  is the vapor density. The kinetic parameter,  $K$ , measures the relative importance of kinetic effects at the interface. The parameter  $\delta$  characterizes the effect of changes in liquid pressure on the local phase-change temperature at the interface.

At the solid–liquid interface the liquid velocity is zero and the nondimensional value of temperature,  $T_0$ , is prescribed as illustrated in Fig. 2b. We note that the heat transfer model used here is appropriate for solid substrates of high thermal conductivity (compared to that of the evaporating liquid) and therefore not applicable to situations such as liquid metal film on a solid metal substrate. A discussion of heat transfer models for arbitrary liquid–solid conductivity ratio can be found e.g. in [37].

Let us now discuss typical values of the key nondimensional parameters for a water film of upstream thickness of 100  $\mu\text{m}$  on a heated surface, relevant e.g. for cooling applications [10,11]. Using physical properties of water at 100  $^\circ\text{C}$  from [38], we obtained a list of values shown in Table 1. The capillary number is clearly small, which justifies the key assumption of the asymptotic theory developed in the next subsection. We also note that the extremely small value of the parameter  $\delta$  may seem to suggest that it can be set to zero. However, since  $\delta$  multiplies the nondimensional disjoining pressure term which becomes very large in ultra-thin films, it is essential to keep it in the equation. Our simulation results described below are not sensitive to changes in  $\delta$  as long as it is sufficiently small, so we use the values of  $\delta$  larger than the one shown in Table 1.

## 2.2. Lubrication-type analysis

In this section we consider the limit of small capillary numbers. In order to obtain physically meaningful solutions we consider distinguished limits when physical quantities, as well as parameters of the problem, scale as certain powers of the capillary number.

Let us assume that the nondimensional Cartesian coordinates  $(x, y)$  shown in Fig. 2a are such that  $y$  is scaled by  $b$  and  $x$  is scaled by  $b/C^{1/3}$ . These scales are commonly used to account for the fact that the length scale in the  $x$ -direction is much larger than the film thickness. In order to derive lubrication-type equations in which viscous stresses balance capillary pressure gradients, the temperature, pressure, velocity component in the vertical direction,  $v$ , the flux and the disjoining pressure are rescaled according to

$$(T - 1, p, v, J, \Pi_0) = C^{2/3}(\bar{T}, \bar{p}, \bar{v}, \bar{J}, \bar{\Pi}), \quad \bar{J} = O(1).$$

The time and evaporation number are rescaled as follows:

$$(t, E) = C^{-1/3}(\bar{t}, \bar{E}).$$

The system of governing equations and boundary conditions is then rescaled and the leading order in  $C$  is retained in a procedure similar to that described in [20]. This leading order system is solved to determine the velocity, pressure and temperature fields within the liquid film, as well as the flux  $J$ . The solution is substituted into the equation of mass conservation at the liquid–vapor interface (7), resulting in the following evolution equation for the film thickness:

$$h_{\bar{t}} + \bar{E}\bar{J} + \frac{1}{3}[h^3(h_{xx} + \Pi)]_x + \sin \alpha h^2 h_x - \frac{M}{2}[h^2(\bar{T})_x]_x = 0, \quad (12)$$

where the interfacial temperature,  $\bar{T}^i$ , can be expressed in terms of the known temperature of the solid surface since according to the scaled heat-conduction equation the temperature profile in the film is linear in  $y$ . The expression for  $\bar{T}^i$  has the following form:

$$\bar{T}^i = \frac{\bar{T}_0 K + \delta h(h_{xx} + \Pi)}{K + h + \beta K h}. \quad (13)$$

The mass flux  $\bar{J}$  can be expressed in terms of the scaled difference between the wall and the saturation temperatures,  $\bar{T}_0$ , in the following form:

$$\bar{J} = \frac{\bar{T}_0 - \delta(h_{xx} + \Pi)(1 + \beta h)}{K + h + \beta K h}. \quad (14)$$

Substituting the last two formulas into Eq. (12) results in the evolution equation for the film thickness:

$$h_{\bar{t}} + \bar{E} \frac{\bar{T}_0 - \delta(h_{xx} + \Pi)(1 + \beta h)}{K + h + \beta K h} + \frac{1}{3}[h^3(h_{xx} + \Pi)]_x + \sin \alpha h^2 h_x - \frac{M}{2} \left[ h^2 \left( \frac{\bar{T}_0 K + \delta h(h_{xx} + \Pi)}{K + h + \beta K h} \right) \right]_x = 0. \quad (15)$$

Eq. (15) relates the rate of change of thickness to the evaporative mass loss (the second term) and the viscous flow rate. The latter has components due to capillary and disjoining pressure gradients, gravity, and thermocapillary stress.

Let us now discuss boundary conditions for Eq. (15). The origin of the coordinate system sketched in Fig. 2a corresponds to the region of uniform film thickness and parallel gravity-driven flow. Let us denote the length of the computational domain by  $L$  and assume that near  $x = L$  the solid surface is macroscopically dry, which in our formulation implies that the height of the interface,  $h(x, \bar{t})$ , is equal to the thickness of the microscopic adsorbed film. In this region the evaporative mass flux is suppressed by London-van-der-Waals forces. Thickness of the equilibrium adsorbed film can be found from the condition of zero mass flux in Eq. (14):

$$\Pi(h_0) = \frac{\bar{T}_0}{\delta(1 + \beta h_0)}. \quad (16)$$

We note that a microscopic film on a macroscopically dry solid surface, often referred to as the precursor film, was discussed in several studies of coating flows [31,32,39], but its thickness was introduced as a parameter of the model. Golovin et al. [40] investigated precursor films of non-uniform thickness by using the balance between van der Waals forces and convective transport, but did not consider the effects of evaporation. In the present work, the thickness of the microscopic film is determined based on the principles of equilibrium thermodynamics as a function of heating conditions, heat transfer in the vapor and material properties of the liquid according to Eq. (16).

Away from the contact line region, the scaled film thickness approaches  $h = 1$  at  $x = 0$  and  $h = h_0$  at  $x = L$ . Additional two boundary conditions have to be specified to ensure that the film is flat at both endpoints of the domain. We follow [20] and choose these in the simple form  $h_x(0) = h_x(L) = 0$ . While alternative formulations have been used in the literature [41], they result in the same local behavior of the interface in the contact line region, as long as the value of  $L$  is large enough and the contact line region is not near one of the endpoints. Both of these assumptions are checked in our numerical simulations.

Let us now specify the temperature profile  $\bar{T}_0(x)$  in Eq. (15). In order to simulate a finite-size heater and preserve the parallel-flow structure of the solution near  $x = 0$  it is convenient to choose the profile in the form

$$\bar{T}_0(x) = \bar{T}_H \left( \frac{1}{2} + \frac{1}{\pi} \tan^{-1} \frac{x - x_0}{l} \right). \quad (17)$$

Here the length scale  $l$  is typically much smaller than  $L$ . In the simulations below we assume  $l = 0.2$ ,  $x_0 = 0.2L$ .

Eq. (15) with the above boundary conditions is solved numerically using finite-difference approach [42]. Standard DVODE solver

**Table 1**

Values of nondimensional parameters used in our formulation.

$C$	$E$	$K$	$\delta$	$T_H$	$M$
$1.6 \times 10^{-3}$	$3.5 \times 10^{-3}$	$4.3 \times 10^{-4}$	$2.7 \times 10^{-7}$	$2.7 \times 10^{-3}$	1.22



[43] is used to describe evolution in time numerically. We start each simulation with an artificial profile which is a step function that jumps from 1 to  $h_0$  at the point  $x = L/2$ .

It should be noted that in the geometry considered here the variation of the film thickness in the vicinity of the apparent contact line is much stronger than that in the rest of the computational domain. Therefore, the mesh in this region should be very fine, whereas much coarser meshes can be used at some distance from the contact line. In order to assure good accuracy of simulations in reasonable computational time, a nonuniform mesh has been used in the present numerical model. For most of our simulations, the fine mesh region extends between  $0.3L$  and  $0.7L$  and the fine mesh size differs from the coarse mesh size by a factor of eight.

### 2.3. Disjoining pressure models

Disjoining pressure in thin liquid films results from simultaneous action of several surface forces giving rise to different components of disjoining pressure, including the molecular component, electrostatic component (existing in ionic solutions) and structural component which has to do with the formation of the so-called hydration layers of polar molecules near interfaces [1].

Let us briefly discuss the models of disjoining pressure used in the present study. The simplest form of the molecular component of disjoining pressure based on the van der Waals forces is given by the following equation [1,2,4]:

$$\Pi(h) = \frac{\varepsilon}{h^3}, \quad (18)$$

where  $\varepsilon$  is a dimensionless constant. If  $\varepsilon > 0$ , then Eq. (18) corresponds to repulsive van der Waals forces and describes a fully wetting liquid in isothermal case.

Using the integrated Lennard-Jones potential for computation of the solid–liquid interaction leads to the following form of the disjoining pressure [21]:

$$\Pi(h) = -\frac{\varepsilon}{h^3} + \frac{a}{h^9}, \quad (19)$$

where both  $\varepsilon$  and  $a$  are dimensionless constants. If  $\varepsilon > 0$  and  $a > 0$ , this form of disjoining pressure describes in isothermal case a meniscus with a finite contact angle which at  $h \rightarrow 0$  asymptotically approaches the adsorbed layer.

The simultaneous action of the molecular and structural components of disjoining pressure is commonly described by the following equation [24]:

$$\Pi(h) = \frac{\varepsilon}{h^3} - d_1 \exp\left(-\frac{h}{d_2}\right). \quad (20)$$

For aqueous films on most common substrates  $\varepsilon > 0$  and  $d_1 > 0$  [44]. The electrostatic component of disjoining pressure is also sometimes approximated by an exponentially decaying function of film thickness.

Wong et al. [25] have chosen the following approximate form for the disjoining pressure:

$$\Pi(h) = \frac{\varepsilon}{h^3} - d_1 \operatorname{sech}^2\left(\frac{h}{d_2} - 2\right), \quad (21)$$

where the constants  $\varepsilon$ ,  $d_1$  and  $d_2$  are positive. The second term of Eq. (21) is not derived based on the theory of disjoining pressure but rather introduced as a simple approximation which can still reproduce the main qualitative features of experimentally observed disjoining pressure curves. This form of disjoining pressure allows one to obtain an analytic expression for an equilibrium contact angle in the isothermal case.

Let us now determine the equilibrium contact angles predicted by each of three disjoining pressure models described above based on the dimensionless form of the Frumkin–Derjaguin Eq. (2):

$$\cos \Phi = 1 + C^{2/3} \int_{h_0}^{\infty} \Pi(h) dh. \quad (22)$$

The thickness of the thin wetting layer  $h_0$  can be computed from the equation  $\Pi(h_0) = 0$ . The asymptotic model used in the present paper implies that the equilibrium contact angle can be written as  $\Phi = C^{1/3} \phi_0$ , where based on (22) the scaled angle  $\phi_0$  is given by

$$\phi_0^2 = -2 \int_{h_0}^{\infty} \Pi(h) dh. \quad (23)$$

For the disjoining pressure model based on the integrated Lennard-Jones potential (Eq. (19)) the thickness of the thin layer can be determined in closed form:

$$h_0 = \left(\frac{a}{\varepsilon}\right)^{1/6}. \quad (24)$$

The scaled equilibrium contact angle can be determined from the following equation:

$$\phi_0^2 = -2 \int_{h_0}^{\infty} \left(-\frac{\varepsilon}{h^3} + \frac{a}{h^9}\right) dh = \frac{3}{4} \varepsilon^{4/3} a^{-1/3}. \quad (25)$$

For the disjoining pressure model described by Eq. (20) a transcendental equation for determination of the thin wetting layer thickness has to be solved numerically. The equilibrium contact angle is found from:

$$\begin{aligned} \phi_0^2 &= -2 \int_{h_0}^{\infty} \left[\frac{\varepsilon}{h^3} - d_1 \exp\left(-\frac{h}{d_2}\right)\right] dh \\ &= 2d_1 d_2 \exp\left(-\frac{h_0}{d_2}\right) - \frac{\varepsilon}{h_0^2}. \end{aligned} \quad (26)$$

Finally, for the disjoining pressure model of Wong et al. (Eq. (21)) the value of  $h_0$  has to be determined numerically, and the contact angle can be computed from the following equation:

$$\begin{aligned} \phi_0^2 &= -2 \int_{h_0}^{\infty} \left[\frac{\varepsilon}{h^3} - d_1 \operatorname{sech}^2\left(\frac{h}{d_2} - 2\right)\right] dh \\ &= 2d_1 d_2 \left[1 + \tanh\left(2 - \frac{h_0}{d_2}\right)\right] - \frac{\varepsilon}{h_0^2}. \end{aligned} \quad (27)$$

Based on the work of Wong et al. [25], the last equation can be approximated as

$$\phi_0 = \sqrt{2d_1 d_2 (1 + \tanh 2)}. \quad (28)$$

## 3. Results and discussion

### 3.1. Steady-state solutions

The mathematical model formulated in the previous section does not include either the position of the contact line or the value of the contact angle as one of its boundary conditions. In fact, the vapor–liquid interface in our model never comes into true contact with the solid substrate. However, the transition region between the macroscopic liquid film and the ultra-thin adsorbed film is highly localized and on macroscale it appears as a line of contact between the interface and the substrate. It is therefore referred to as an apparent contact line here and below.

Let us first discuss the case when the vapor–liquid interface is steady. Our numerical simulations indicate that this regime can be achieved by making evaporation sufficiently high, so that the gravity-driven flow down toward the apparent contact line region

is balanced by evaporative mass loss there. A typical steady-state solution in this regime is illustrated in Fig. 3; both interface profile and the slope are shown in the plot. The liquid film is flat near the left boundary of the computational domain and forms a well-defined capillary ridge near the apparent contact line. This shape is in qualitative agreement with previous numerical and experimental studies of both isothermal and evaporating gravity-driven films [7,20,32,33]. It is clear from Fig. 3 (dashed line) that the absolute value of the slope reaches a maximum near the apparent contact line and then drops sharply to zero in the adsorbed film. This maximum value is referred to as a scaled apparent contact angle and denoted by  $\phi_0$ . The actual apparent contact angle  $\Phi$  can be easily found using  $\Phi = C^{1/3} \phi_0$  (note that the difference between  $\tan \Phi$  and  $\Phi$  is negligible in the asymptotic limit considered here).

Since the heater temperature is a natural control parameter in experiments, let us investigate how the scaled apparent contact angle  $\phi_0$  depends on  $\bar{T}_H$ . We choose  $\alpha = \pi/4$  and the range of  $\bar{T}_H$  over which all disjoining pressure models considered result in steady-state solutions (such solutions fail to exist for small  $\bar{T}_H$  when evaporation can no longer balance the downward flow). Typical plots of  $\phi_0$  as a function of scaled heater temperature for different disjoining pressure models are shown in Fig. 4. The contact angles increase with the heater temperature, which is consistent with experimental studies of steady evaporating contact lines. Note that the liquid which is perfectly wetting under the isothermal conditions, i.e. is characterized by disjoining pressure having only the van der Waals component, shows a non-zero value of the apparent contact angle under evaporation conditions (see the dotted line). The two-component disjoining pressure models allow description of liquids which are partially wetting under the isothermal conditions. Fig. 4 shows scaled apparent contact angles on heated surfaces for the liquid-wall pairs with disjoining pressure given by the model of Wong et al. [25] (dashed line), the model of Sharma and Jameel [24] (solid line), and the integrated Lennard-Jones model [21] (dotted-dashed line). The behavior of the solid and dashed lines in Fig. 4 is clearly very similar despite the fact that they correspond to different disjoining pressure curves. This suggests that the contact angle is likely to be a function of some integral quantities taken over the apparent contact line region and not of the details of the interface shape and disjoining pressure there. However, it is evident that the Frumkin–Derjaguin theory cannot be directly applied for prediction of apparent contact angles in the presence of evaporation, since this angle is a strong function of the evaporation-related parameters which are not accounted for in the Frumkin–Derjaguin equation. We pro-

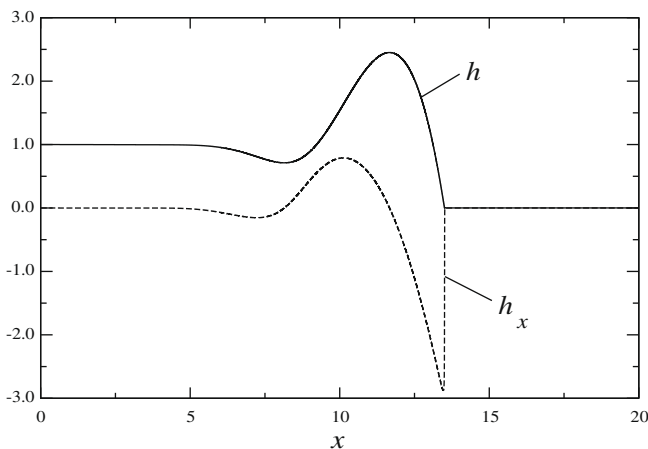


Fig. 3. Typical steady interface shape (solid line) and its slope (dashed line) for  $\alpha = \pi/4$ ,  $\bar{T}_H = 0.5$ ,  $K = 10^{-3}$ ,  $\varepsilon = 10^{-4}$ ,  $\delta = 10^{-5}$ ,  $\bar{E} = 0.04$ ,  $M = \beta = d_1 = 0$ .

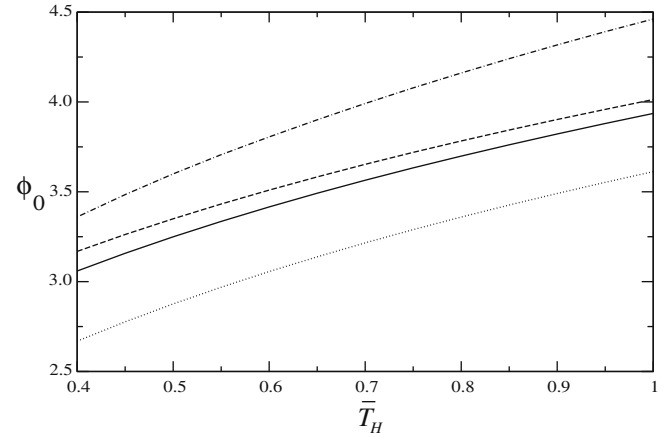


Fig. 4. Scaled apparent contact angles in the steady-state regime as functions of the heater temperature for  $\alpha = \pi/4$ ,  $\bar{E} = 0.04$ ,  $\delta = 10^{-5}$ ,  $K = 10^{-3}$ ,  $M = \beta = 0$ , and different disjoining pressure models: Eq. (18) with  $\varepsilon = 10^{-4}$  (dotted line), Eq. (21) with  $\varepsilon = 10^{-4}$ ,  $d_1 = 100$ ,  $d_2 = 0.01$  (dashed line), Eq. (20) with  $\varepsilon = 10^{-4}$ ,  $d_1 = 100$ ,  $d_2 = 0.02$  (solid line), Eq. (19) with  $\varepsilon = 10^{-4}$ ,  $a = 10^{-16}$  (dot-dashed line).

pose a generalization of this equation for the case with evaporation, derived as follows. We subtract the expression for the interfacial mass flux, Eq. (14), for  $\beta = 0$  and multiplied by  $K$ , from the expression for the interfacial temperature, Eq. (13), also for  $\beta = 0$ , and obtain

$$\bar{T}^i - \bar{J}K = \delta(h_{xx} + \Pi). \quad (29)$$

We multiply this equation by  $h_x$  and integrate it in  $x$  from a point in the adsorbed film to a point outside the transition zone (a macroscopic value of  $h$ ). This results in the following expression for computation of the scaled apparent contact angle:

$$\phi_0^2 = -2 \int_{h_0}^{\infty} \Pi(h) dh + \frac{2}{\delta} \int_{h_0}^{\infty} (\bar{T}^i - \bar{J}K) dh. \quad (30)$$

Thus, the details of the complicated coupling between heat transfer and fluid flow actually only enter the expression for contact angle through integrals of the interfacial temperature and the evaporative flux over the transition region. Let us investigate the relative importance of the two integrals in Eq. (30). Consider the disjoining pressure model given by Eq. (21). For this model the absolute value of the first integral in (30), denoted by  $I_1$ , can be expressed analytically since

$$I_1 = 2 \int_{h_0}^{\infty} \Pi(h) dh = \frac{\varepsilon}{h_0^2} - 2d_1d_2 \left[ 1 + \tanh \left( 2 - \frac{h_0}{d_2} \right) \right]. \quad (31)$$

In contrast to the isothermal meniscus situation discussed by Wong et al. [25], the term  $\frac{\varepsilon}{h_0^2}$  is not negligible here due to much smaller values of the dimensional ultra-thin film thickness.

The absolute value of the second integral in (30) cannot be found analytically, so we approximate it numerically by computing

$$I_2 = \frac{2}{\delta} \int_{h_0}^{h^*} (\bar{T}^i - \bar{J}K) dh, \quad (32)$$

where  $h^*$  is the film thickness at which the maximum slope angle is attained in our numerical solution. Based on (30), an approximation to the value of the apparent contact angle can be written as  $\phi_0 \approx \sqrt{I_2 - I_1}$ . The quantities  $I_1$  and  $I_2$  are plotted in Fig. 5. The absolute value of integral of the disjoining pressure curve,  $I_1$ , is much larger than that in the isothermal case due to smaller values of the ultra-thin film thickness,  $h_0$ . Moreover, for the studied range of the wall temperatures  $I_1$  is positive, whereas it is negative for

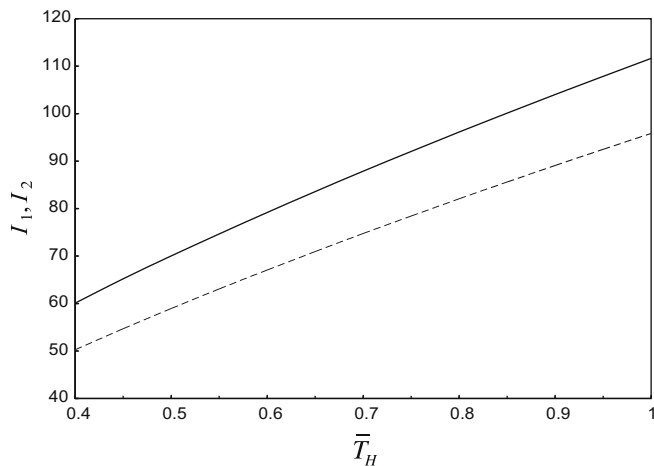


**Fig. 5.** The absolute values of the two integrals in the generalized Frumkin–Derjaguin theory for the disjoining pressure model of Eq. (21) with  $\varepsilon = 10^{-4}$ ,  $d_1 = 100$ ,  $d_2 = 0.01$ . Dashed line:  $I_1$  (defined by Eq. (31)), solid line:  $I_2$  (defined by Eq. (32)).

the isothermal case. This integral can be balanced by another large quantity,  $I_2$ , to give a value of the contact angle close to unity. While this value is not much different from the isothermal one, it is important to emphasize that the contact angle in our model depends on both disjoining pressure and heat transfer, as opposed to an interplay between different components of disjoining pressure. To further contrast our results with the isothermal case, we note that the value of  $\phi_0$  can become small when the values of  $I_1$  and  $I_2$  in Fig. 5 are getting close to each other. If the heater temperature is reduced below the point corresponding to  $I_1 = I_2$ , steady-state solutions are no longer possible, since evaporation in this regime is not strong enough to compensate for the gravity-driven downward flow of the liquid.

### 3.2. Dynamic contact angles

As the scaled evaporation number  $\bar{E}$  is reduced, the static solutions are no longer possible except for very small slope angles. However, a quasi-steady regime can be established such that the dimensionless contact line speed  $u_{CL}$  is approximately constant and the interface shape in the vicinity of the contact line does not change with time. By changing the inclination angle  $\alpha$ , one can investigate a wide range of values of  $u_{CL}$ . Since the focus of the present study is on the apparent contact angles, let us plot  $\phi$ , the maximum absolute value of the slope for the moving interface, as a function of contact line velocity. Several dynamic contact line models predict that  $\phi^3 - \phi_0^3 \sim u_{CL}$ , so it is natural to plot the data in  $\phi^3 - u_{CL}$  coordinates. The result for  $K = 10^{-3}$ ,  $\delta = 10^{-5}$ ,  $M = \beta = 0$ , the exponential model of disjoining pressure given by Eq. (20) with  $\varepsilon = 10^{-4}$ ,  $d_1 = 100$ ,  $d_2 = 0.02$ , and different values of  $\bar{E}$  and  $T_H$  is shown in Fig. 6. The plot illustrates that the linear dependence of  $\phi^3$  on the contact line speed in this quasi-steady regime can still be observed despite the effects of evaporation. Note that even though the values of scaled evaporation number are small, in dimensional terms they correspond to rather substantial evaporative mass loss. Yet, this mass loss apparently does not alter the structure of the flow enough to result in the breakdown of the linear dependence of  $\phi^3$  on  $u_{CL}$ .

By comparing different lines in Fig. 6, one can make the following observations. First, similar to the static case, the dynamic contact angle increases as the evaporative mass loss is increased, in accordance with the well-known physical idea of superposition of the effects of viscous flow and evaporation introduced by Ander-

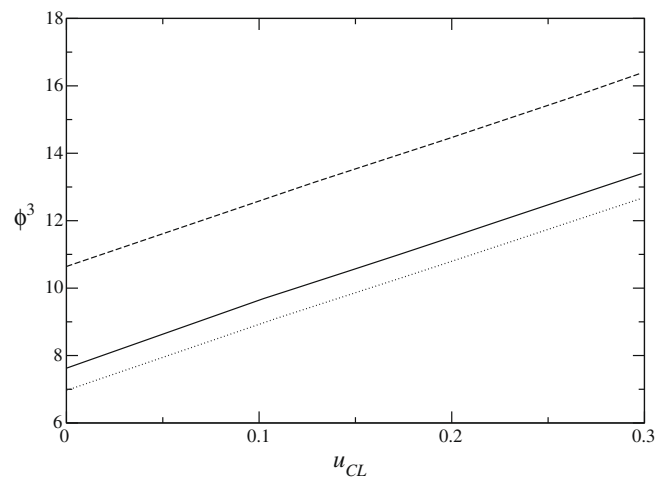


**Fig. 6.** Scaled apparent contact angle versus the scaled contact line speed for  $T_H = 1$ ,  $\bar{E} = 0.001$  (solid line),  $\bar{E} = 0.002$  (dashed line), and  $\bar{E} = 0.002$ ,  $T_H = 0.5$  (dotted line). The disjoining pressure is given by Eq. (20) with  $\varepsilon = 10^{-4}$ ,  $d_1 = 100$ ,  $d_2 = 0.02$ .

son and Davis [45]. Second, we observe that the slopes of all three lines are not very different despite the fact that the heating conditions differ significantly. It has been suggested that the slope of the  $\phi^3$  versus  $u_{CL}$  line is proportional to logarithm of the ratio of macroscopic and microscopic length scales of the problem [46], which does not show a strong dependence on the heating conditions.

While the Tanner's law is well-established for relatively slow motion of contact lines, there has been increasing experimental evidence that for rapid motion the local contact angle may depend on the history of the system and does not follow the dependence based on a single  $\phi(u_{CL})$  curve [47]. The models which require a specification of contact angle condition, either constant or a function of contact line speed, may not be adequate for describing this situation. However, in our model the contact angle is not prescribed in any way, and therefore we expect that our approach can capture the non-local behavior of the contact lines. To illustrate that this is indeed the case, let us study the dynamic response of the interface to instantaneous changes in the heater temperature. Let us use the exponential disjoining pressure model ( $d_1 = 100$ ,  $d_2 = 0.02$ ) with all other parameter values being the same as specified in caption to Fig. 4. We started by running the simulation with  $T_H = 1$  until the system reached the steady state. Then, the value of  $T_H$  is decreased instantaneously to 0.5 and the slope angle is recorded as a function of time, shown by the solid line in Fig. 7. The local contact line velocity is also recorded and then used to predict the contact angle dynamics from the linear relationship between  $\phi^3$  and  $u_{CL}$  (dashed line). While the comparison between the two curves is excellent for larger times, there is a small discrepancy over the time interval on the order of 10, indicating that the simple linear model does not give accurate results there.

### 3.3. Marangoni stresses

The interfacial temperature in our model deviates from the equilibrium saturation temperature, especially in the apparent contact line region. Thus, it is natural to expect that thermocapillary stresses at the interface can affect the flow in the liquid. In the model formulated in Section 2, these stresses are taken into account; their significance is measured by the modified Marangoni number,  $M = \gamma T_S^* / \sigma_0$ . In the simulations discussed so far, thermocapillary stresses were neglected by taking the value of  $M$  to be zero. Let us now investigate how the values of apparent contact

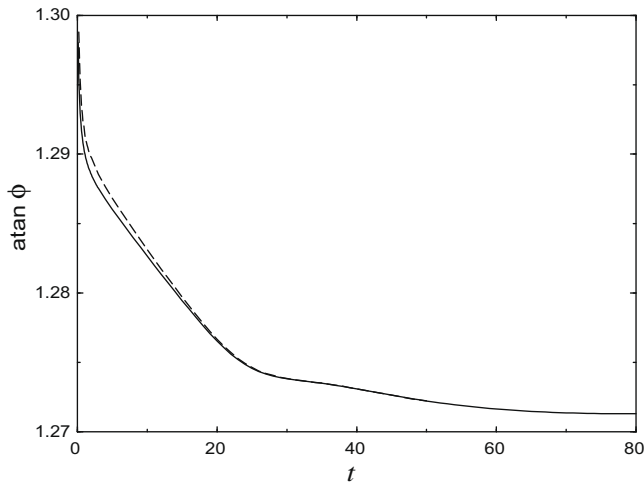


**Fig. 7.** The slope angle in scaled coordinates as a function of time following a rapid change of heater temperature from  $\bar{T}_H = 1$  to  $\bar{T}_H = 0.5$ , recorded from the simulations (solid line) and predicted based on the Tanner's law (dashed line).

angles are affected by the thermocapillary stresses by running the simulations for  $M = 1$ , which is a realistic value encountered in experiments. According to Eq. (11), the degree of non-equilibrium

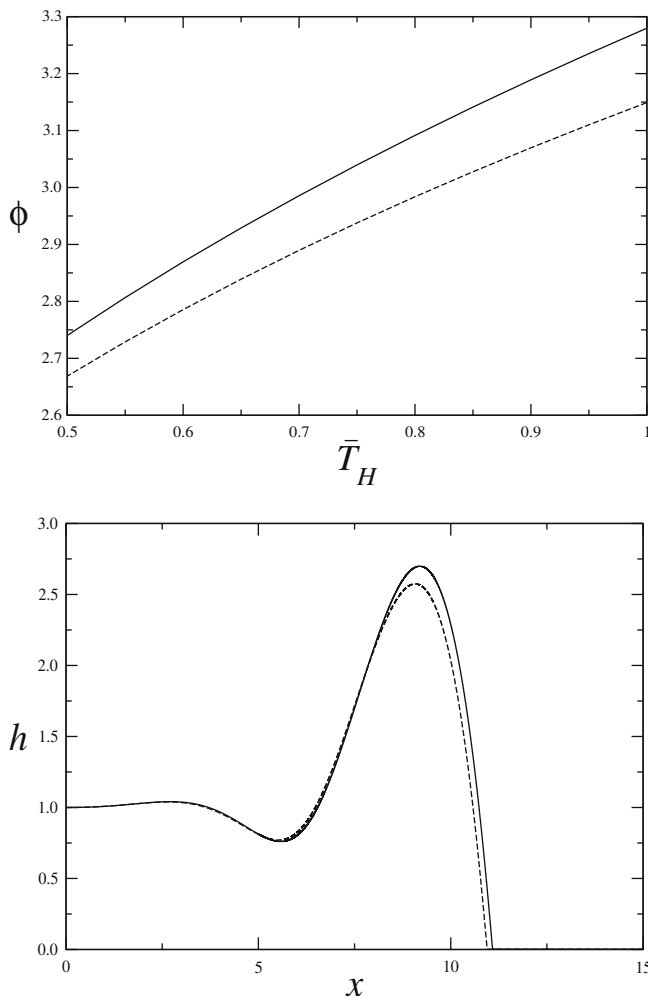


**Fig. 8.** (top) The scaled apparent contact angle as a function of scaled temperature for  $M = 0$  (dashed line) and  $M = 1$  (solid line); (bottom) Steady shapes of the vapor-liquid interface at  $\bar{T}_H = 0.8$  for  $M = 0$  (dashed line) and  $M = 1$  (solid line).

at the interface and therefore the value of the interfacial temperature depend on the value of the kinetic parameter  $K$ . Based on our simulations, the effect of Marangoni stresses turns out to be very small for a range of values of  $K$  below  $10^{-3}$ , which justifies the approximation of  $M = 0$  used in the previous subsections. We note that this conclusion would not be applicable to locally heated films of nonvolatile liquids [48,49].

The role of Marangoni stresses increases with increasing of the kinetic parameter  $K$ . To illustrate the effect of these stresses, we plot the apparent contact angle in the steady regime as a function of heater temperature (see Fig. 8, top). The computations have been performed for  $K = 0.01$ ,  $\delta = 10^{-5}$ ,  $\beta = 0.1$ ,  $\bar{E} = 0.04$  and  $\alpha = \pi/4$ . The exponential disjoining pressure model with  $\varepsilon = 10^{-4}$ ,  $d_1 = 100$  and  $d_2 = 0.02$  has been used. The result shown in Fig. 8 indicates that the Marangoni stresses result in an increase of the value of the contact angle over a range of heater temperatures. This can be explained by noticing that the thermocapillary stresses tend to move liquid away from the hotter regions near the ultra-thin films and therefore result in steepening of the interface profile there. To illustrate this we plot the steady interface shapes for  $M = 1$  (solid line) and  $M = 0$  (dashed line) at a specific heater temperature ( $\bar{T}_H = 0.8$ ) in Fig. 8(bottom). The plot also shows that Marangoni stresses result in more significant accumulation of liquid in the capillary ridge behind the contact line than predicted by the model with  $M = 0$ .

The correction due to Marangoni stresses (the difference between the two curves in Fig. 8, top) increases slightly for higher values of the scaled heater temperature,  $\bar{T}_H$ .

#### 4. Conclusions

We investigated the flow and evaporation of a thin liquid film on an inclined surface for different models of disjoining pressure. The focus of the study is on understanding the dependence of the apparent contact angle on the wetting properties and the rate of evaporation. The apparent contact angle is defined as the maximum value of the slope angle in the transition region between the macroscopic film and the ultra-thin adsorbed film which covers the substrate.

We first investigated the regime in which the gravity-driven flow toward the apparent contact line is balanced by evaporative mass loss there, so that the overall configuration is steady. We found that the apparent contact angle in this regime increases with temperature over a wide range of wetting conditions. While in the isothermal case the contact angle is determined by the interplay between two different components of disjoining pressure, in the presence of evaporation the contact angle is much less sensitive to the details of disjoining pressure curves and depends on the intensity of heating. Therefore, the classical Frumkin–Derjaguin theory does not give accurate predictions of the value of static contact angle. A generalization of this theory is developed, which expresses the static contact angle in terms of integrals of the disjoining pressure curve, interfacial temperature and mass flux over the apparent contact line region. The effect of thermocapillary forces is also studied and is shown to result in slight increase of the values of the apparent contact angle.

As the evaporation intensity is reduced for a fixed slope angle, a different type of solution is possible, with contact line speed approaching a constant (but non-zero) value. The dynamic contact angle in this regime follows the Tanner's law (i.e. the cube of the contact angle is a linear function of the contact line speed) for a range of evaporation conditions. However, the linear dependence does not accurately predict the contact angle versus speed relationship as the time scale of the interface evolution is decreased. Any model based on contact angle boundary condition cannot ac-



count for non-local effects, even if a more complicated form of  $\phi(u_{cl})$  is used instead of the simple Tanner's law. Our approach to describing the contact line as a transition region is free from this limitation and is therefore equally suitable for describing either slow or fast evolution of dynamic contact lines. This is illustrated by studies of the dynamic response of the contact angle to rapid changes in the heater temperature. The linear model slightly overpredicts the value of apparent contact angle under the conditions when the interface shape changes rapidly.

## Acknowledgment

This work was partially supported by the Alexander von Humboldt Foundation.

## References

- [1] B.V. Derjaguin, N.V. Churaev, V.M. Muller, *Surface Forces*, Plenum Press, New York, 1987.
- [2] J. Israelachvili, *Intermolecular and Surface Forces*, Academic, San Diego, 1992.
- [3] M. Potash, P.C. Wayner, *Int. J. Heat Mass Transfer* 15 (1972) 1851.
- [4] S. Moosman, G.M. Homsy, *J. Colloid Interface Sci.* 73 (1980) 212.
- [5] S. DasGupta, J.A. Shoenberg, I.Y. Kim, P.C. Wayner, *J. Colloid Interface Sci.* 157 (1993) 332.
- [6] S.J.S. Morris, *J. Fluid Mech.* (2001) 432 1.
- [7] A.V. Lyushnin, A.A. Golovin, L.M. Pismen, *Phys. Rev. E* 65 (2002) 021602.
- [8] P. Stephan, C.A. Busse, *Int. J. Heat Mass Transfer* 35 (2) (1992) 383.
- [9] G.P. Celata, M. Cumo, A. Mariani, L. Saraceno, *Heat Mass Transfer* 45 (2009) 1029.
- [10] O.A. Kabov, *Thermophys. Aeromech.* 7 (2000) 513.
- [11] O.A. Kabov, E.A. Chinnov, *High Temp.* 39 (2001) 703.
- [12] C. Sodtke, V.S. Ajaev, P. Stephan, *J. Fluid Mech.* 610 (2008) 343.
- [13] D. Wu, G.P. Peterson, *J. Thermophys. Heat Transfer* 5 (1991) 129.
- [14] A. Mukherjee, S.G. Kandlikar, *Microfluid. Nanofluid.* 1 (2005) 137.
- [15] O.V. Voinov, *Izv. Akad. Nauk SSSR Mekh. Zhid. i Gaza* 5 (1976) 76.
- [16] L.H. Tanner, *J. Phys. D: Appl. Phys.* 12 (1979) 1473.
- [17] R.L. Hoffman, *J. Colloid Interface Sci.* 50 (1975) 228.
- [18] S.F. Kistler, *Hydrodynamics of wetting*, in: J.C. Berg (Ed.), *Wettability*, vol. 311, Marcel Dekker, New York, 1993.
- [19] V.S. Ajaev, G.M. Homsy, S. Morris, *J. Colloid Interface Sci.* 254 (2002) 346.
- [20] V.S. Ajaev, *J. Colloid Interface Sci.* 280 (2004) 165.
- [21] V.S. Mitlin, N.V. Petviashvili, *Phys. Lett. A* 192 (1994) 323.
- [22] A. Oron, S.G. Bankoff, *J. Colloid Interface Sci.* 218 (1999) 152.
- [23] K.B. Glasner, T.P. Witelski, *Phys. Rev. E* 67 (2003) 016302.
- [24] A. Sharma, A.T. Jameel, *J. Colloid Interface Sci.* 161 (1993) 190.
- [25] H. Wong, S. Morris, C.J. Radke, *J. Colloid Interface Sci.* 148 (1992) 317.
- [26] C.A. Miller, E. Ruckenstein, *J. Colloid Interface Sci.* 48 (1974) 368.
- [27] L.M. Hocking, *Phys. Fluids A* 5 (1993) 793.
- [28] A. Indeikina, H.-C. Chang, *A molecular theory for dynamic contact angles*, preprint, 1999.
- [29] Q. Wu, H. Wong, *J. Fluid Mech.* 506 (2004) 157.
- [30] A.N. Frumkin, *Zh. Fiz. Khim.* 12 (1938) 337.
- [31] L. Kondic, A.L. Bertozzi, *Phys. Fluids* 11 (1999) 3560.
- [32] M.H. Eres, L.W. Schwartz, R.V. Roy, *Phys. Fluids* 12 (2000) 1278.
- [33] R. Goodwin, G.M. Homsy, *Phys. Fluids A* 3 (1991) 515.
- [34] A. Mazouchi, C.M. Gramlich, G.M. Homsy, *Phys. Fluids* 16 (2004) 1647.
- [35] J.P. Burelbach, S.G. Bankoff, S.H. Davis, *J. Fluid Mech.* 195 (1988) 463.
- [36] V.S. Ajaev, G.M. Homsy, *J. Colloid Interface Sci.* 240 (2001) 259.
- [37] S.J.S. Morris, *Proc. Roy. Soc. Lond. A* 460 (2004) 2487.
- [38] *VDI-Waermeatlas*, 9th ed., Springer, Berlin, 2002.
- [39] S.M. Troian, E. Herbolzheimer, S.A. Safran, J.F. Joanny, *Europhys. Lett.* 10 (1989) 25.
- [40] A.A. Golovin, B.Y. Rubinstein, L.M. Pismen, *Langmuir* 17 (2001) 3930.
- [41] L. Kondic, J. Diez, *Phys. Fluids* 13 (2001) 3168.
- [42] L. Zhornitskaya, A.L. Bertozzi, *SIAM J. Numer. Anal.* 37 (2000) 523.
- [43] P.N. Brown, C.D. Byrne, A.C. Hindmarsh, *SIAM J. Sci. Stat. Comput.* 10 (1989) 1038.
- [44] A.S. Padmakar, K. Kargupta, A. Sharma, *J. Chem. Phys.* 110 (1999) 1735.
- [45] D.M. Anderson, S.H. Davis, *Phys. Fluids* 7 (1995) 248.
- [46] L. Leger, J.-F. Joanny, *Rep. Prog. Phys.* 55 (1992) 431.
- [47] J. Lei, M. Perlin, W.W. Schultz, *Phys. Fluids* 16 (2004) 748.
- [48] C.M. Gramlich, C.M. Kalliadasis, G.M. Homsy, C. Messer, *Phys. Fluids* 14 (2002) 1841.
- [49] N. Garnier, R.O. Grigoriev, M.F. Schatz, *Phys. Rev. Lett.* 91 (2003) 054501.